Magnetism at an iridate/manganite interface: Influence of strong spin-orbit interaction

G. A. Ovsyannikov ●,[1,*] T. A. Shaikhulov,[1] K. L. Stankevich,[1] Yu. Khaydukov,[2,3] and N. V. Andreev[4]

[1]*Kotel'nikov Institute of Radio Engineering and Electronics Russian Academy of Sciences, Mokhovaya str. 11–7, 125009 Moscow, Russia*
[2]*Max Planck Institute for Solid State Research, Heisenbergstraße 1, 70569 Stuttgart, Germany*
[3]*Max Planck Society Outstation at the MLZ, Garching, Germany*
[4]*National University of Science & Technology (MISIS), Lenin av. 4, 119991 Moscow, Russia*

A comprehensive study of electron and magnetic properties and spin transport in the epitaxial manganite/iridate heterostructure was carried out by using of the x-ray, dc resistance measurements, ferromagnetic resonance at microwaves, polarized neutron reflectivity, and spin-current transport. Epitaxial growth of the heterostructure proceeded according to the "cube-to-cube" mechanism with a small lattice turn. The dc current measurement indicates the presence of a conduction channel at the iridate/manganite interface due to the charge leak from iridate making it hole doped, while the manganite side can be doped by electron. This is confirmed by the first-principles calculations based on density-functional theory [S. Bhowal and S. Satpathy, AIP Conf. Proc. **2005**, 020007 (2018)], which showed a charge transfer at the interface from the half-filled spin-orbit entangled $J_{\mathrm{eff}} = 1/2$ state of the iridate to the empty $e^{\uparrow}g$ states of manganite. The neutron-scattering data show the turn of magnetization vector of the heterostructure by $26°$ towards the external field with temperature reduction down to 10 K. An additional ferromagnetic state that appears at $T < 100\,\mathrm{K}$ indicates an emergence of ferromagnetism at the interface of the paramagnetic $SrIrO_3$ film and ferromagnetic manganite. We measured the dc voltage that occurs on the $SrIrO_3$ film due to spin pumping and anisotropic magnetoresistance in the heterostructure.

I. INTRODUCTION

Transition-metal oxides (TMOs) which differ from binary oxides like SiO_2 to more complex compounds contents are nowadays a subject of intense activities in condensed-matter physics.

The 3d TMOs have various functionalities, including ferromagnetism due to the presence of the strong electron-electron correlation energy (U) [1,2]. However, the spin-orbit interactions (with energy E_{SO}) are generally weak or not significant in 3d TMOs. On the other hand, 5d TMOs attract a great deal of interest due to the presence of the strong spin-orbit interactions, which coexist along with the electron-electron interaction. In 5d transition metals, $E_{\mathrm{SO}} \approx 0.4\,\mathrm{V}$ is many times higher than E_{SO} 3d transition metals and it is comparable with the energy of electron correlations $U \sim 0.5\,\mathrm{eV}$. In theoretical works [3,4] it has been shown that the combination of spin-orbit interaction and the electron-electron interaction can lead to emergence of many new quantum states of matter, such as topological Mott insulator [5,6], quantum spin Hall effect, quantum anomalous Hall effect [7–9], Weyl semimetal [10], and even a high-T_C superconductor [11,12]. The contact between 3d and 5d TMOs provides a unique interface where both electron-electron and spin-orbit interactions are realized, which is not possible in the well-studied 3d/3d TMO interfaces [13–17]. The reconstructed magnetic anisotropy and the strong spin-orbital interactions indicate that the 3d/5d

interfaces can be used as objects for magnetic texture and topological phenomena observations [18]. At the interface of such materials with a ferromagnetic, the topological symmetry in the region of interface can be violated and a gap in the excitation spectrum can be created, which in turn can result in magnetoelectric effects. These interfaces provide the ideal candidates to search for novel magnetic textures and topological phenomena. Moreover, due to the inherent mixture of the spin and orbital degrees of freedom in the 5d TMOs, these heterostructures also provide the potential pathways to achieve the electric field control of magnetism through the mechanisms that have not been demonstrated in 3d/3d heterostructures. The current research is still in the early stage and it is limited by few systems, and more systematic investigations are highly desired to fully unravel the unique role of 5d TMOs.

Iridate $SrIrO_3$ crystal has a slightly distorted $SrRuO_3$-type orthorhombic structure ($a = 0.560\,\mathrm{nm}$, $b = 0.558\,\mathrm{nm}$, $c = 0.789\,\mathrm{nm}$) of the *Pbnm* space group [19]. Thin $SrIrO_3$ epitaxial films form a perovskite structure during the film growth. Such films can be described as a distorted pseudocubic with a constant 0.396 nm [20–28]. Due to the crystal structure similar to manganites, the epitaxial films of the $SrIrO_3$ iridate can be an excellent component for the growth of heterostructures with manganites. The low-energy state of 5d electrons of the $Ir4^+$ state is half full ($J_{\mathrm{eff}} = 1/2$ state) due to the strong interaction of the spin and orbital degrees of freedom and therefore the energy spectrum in the 5d TMOs differs significantly from 3d manganites [29]. Experimentally, $SrIrO_3$ is a paramagnetic metal which is transformed to a paramagnetic insulator below the transition temperature $T_{\mathrm{MI}} = 44\,\mathrm{K}$ [30].

*gena@hitech.cplire.ru

Good crystalline correspondence between $SrIrO_3$ epitaxial films and other perovskites allows creation of $SrIrO_3/La_{1-x}Sr_xMnO_3$ superlattices with different x values [15,31], $SrIrO_3/SrTiO_3$ [14,32] and $SrIrO_3/LaMnO_3$ [33]. In the $SrMnO_3/SrIrO_3$ superlattice [17] the interface forms a nonpolar boundary. Hybridization of Mn and Ir orbitals has led to the emergence of the ferromagnetism in antiferromagnetic $SrMnO_3$ [17]. In superlattice the thickness of the $SrIrO_3$ layer varies with the axis of easy magnetization of the manganite layer rotating between the crystallographic directions: [110] $La_{0.7}Sr_{0.3}MnO_3$ and [001] $La_{0.7}Sr_{0.3}MnO_3$ [15,31].

Recently the transport properties and ferromagnetic resonance spectra of heterostructure $La_{0.7}Sr_{0.3}MnO_3/SrIrO_3$ have been studied [34,35]. The parameters of heterostructure are compared with the properties of the autonomous films of iridate and manganite. The linewidth of ferromagnetic resonance spectrum increases and the resonance field decreases at lower temperatures [34,35]. The effect of spin pumping on magnetic damping has been observed [34,35].

In this paper we present the results of the growth of an epitaxial heterostructure of an iridate with strong spin-orbit interaction ($SrIrO_3$) and ferromagnetic manganite ($La_{0.7}Sr_{0.3}MnO_3$), which has a Curie temperature above room temperature. We present the results of electrical, magnetic, and neutron measurements of the heterostructure. The remaining parts of the paper are organized as follows. The heterostructure fabrication and x-ray data are presented in Sec. II. This shows the growth of the heterostructure proceeding according to the "cube-to-cube" mechanism with the small lattice turn. This is followed by dc resistance measurement for single-layer films and heterostructures (Sec. III). The charge transport at the interface in the heterostructure differs significantly from both single-layer films such as $SrIrO_3$ and $La_{0.7}Sr_{0.3}MnO_3$ and Pt transport. Data measured by superconducting quantum interference device (SQUID) and polarized neutron reflectivity are presented in Sec. IV. The temperature dependence of the saturation magnetization of the heterostructure and neutron data corresponds well to the mean-field approximation. The neutron experiment shows the turn of the magnetic vector of the heterostructure on $26°$ at the temperature below 10 K.

Ferromagnetic resonance was measured for the heterostructure with temperature variation. An additional ferromagnetic ordering was observed in the heterostructure at $T \leqslant 100$ K (Sec. V). Finally, in Sec. VI the voltage induced by the spin current aroused across the interface in heterostructure during ferromagnetic resonance was compared to the voltage induced by the anisotropic magnetoresistance. The summary of the paper is presented in Sec. VII. The method of determining the magnetic parameters of the heterostructure is based on the angular dependence of FMR spectrum and it is described in the Appendix.

II. HETEROSTRUCTURE FABRICATION AND X-RAY DATA

The heterostructures were obtained by magnetron sputtering on a neodymium gallium substrate with an orientation (110) $NdGaO_3$ (NGO) at a temperature $T = 820°C$ and an oxygen pressure of 0.7 mbar for lanthanum strontium man-
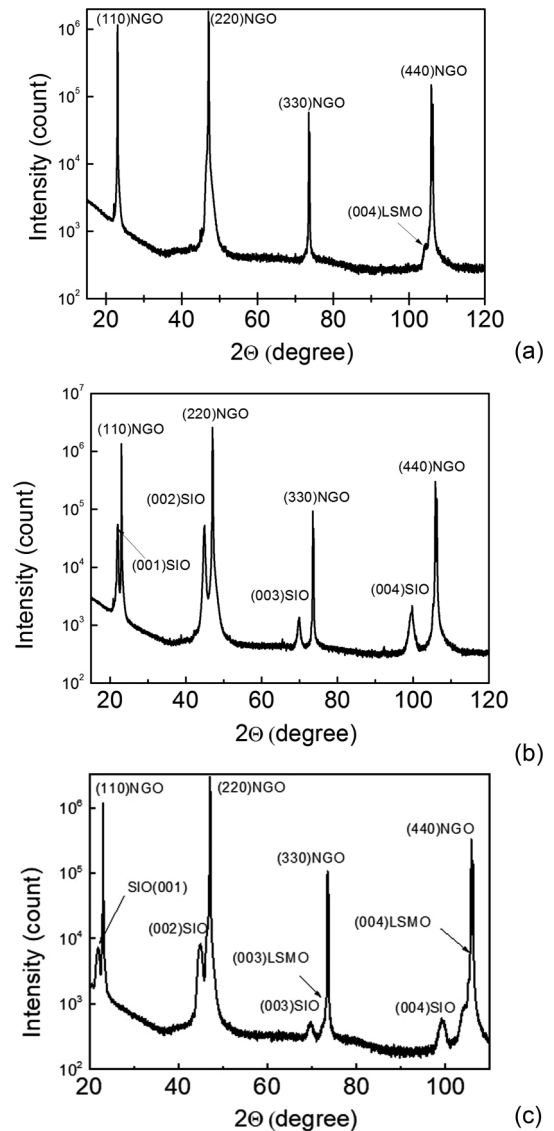
FIG. 1. X-ray 2θ-ω scans for autonomous films: (a) SIO and (b) LSMO, as well as (c) SIO/LSMO heterostructure. All films deposited on (110) NGO substrate

ganite $La_{0.7}Sr_{0.3}MnO_3$ (LSMO) film and $T = 770°C$ and a pressure of 0.3 mbar for the iridate $SrIrO_3$ (SIO). After deposition, the films were cooled to $600°C$ in 1 atm oxygen for 10 min and then were cooled down to room temperature in 20 min. The film thicknesses varied from 5 to 50 nm. We used the deposition time to control the thickness of the SIO film after measuring the film thickness using the Alfa-Step technique [36].

The crystal structure of thin films of SIO and LSMO and heterostructures are characterized by x-ray diffraction (Bruker Discover VIII using $CuK\alpha$ radiation). Figure 1(a) shows the 2θ-ω scan of the SIO thin film. The observed peaks are related to many reflections from the plane (110) NGO of substrate and from the (001)SIO film (the pseudocubic notation). This suggests that the film is out-of-plane orientated (001)SIO∥(110)NGO. The same pattern can be seen for the thin-film LSMO [Fig. 1(b)]. If we describe

(a)

(b)
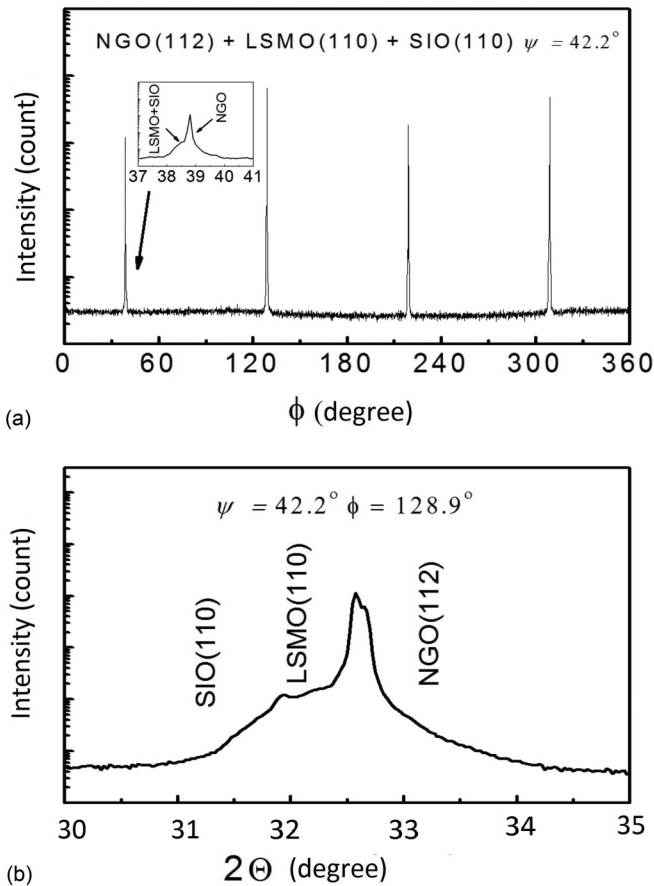
FIG. 2. (a) XRD ϕ-scan at $\psi = 42.2$ for the SIO/LSMO heterostructure tilted to (112) NGO; inset shows enchantment of single peak. (b) 2θ-ω scan of the heterostructure for tilted configuration $\omega = 42.2°$ and $\phi = 128.9°$.

the LSMO lattice as a pseudocubic with the parameter $a = 0.389$ nm [36], then the peaks visible reveal that the film is also out-of-plane-oriented (001)LSMO‖(110)NGO. The superposition of single-layer films scans is shown on the 2θ-ω scan of heterostructure SIO/LSMO deposited on NGO substrate [Fig. 1(c)]. The out-of-plane lattice parameter in the LSMO film does not change significantly with growth in the heterostructure remaining similar as for an autonomous film $d_{LSMO} = 0.388$ nm. A slight change is observed in the out-of-plane lattice parameter from the single-layer SIO film from $d_{SIO}^A = 0.403$ nm to $d_{SIO} = 0.404$ nm for the heterostructure.

Figure 2(a) shows x-ray diffraction (XRD) ϕ-scan at tilt angle $\psi = 42.2°$ and $2\theta = 38.5°$ angle for the SIO/LSMO heterostructure for the (112) NGO plane. In addition, with the four strong peaks from the substrate spaced at almost 90° (weak orthorhombic of the substrate NGO) we can observe the reflections from the planes (110)SIO and (110)LSMO planes, peaks converge and are displaced from the substrate peaks by approximately 0.3° [see inset of Fig. 2(b)]. The corresponding 2θ-ω scan with $\psi = 42.2°$ and $\phi = 128.9°$ is presented in Fig. 2(b). Thus we can conclude that the growth of the heterostructure proceeded according to the cube-to-cube mechanism with the small lattice turn. The epitaxial relationships are as following: (001)SIO‖(001)LSMO‖(110)NGO
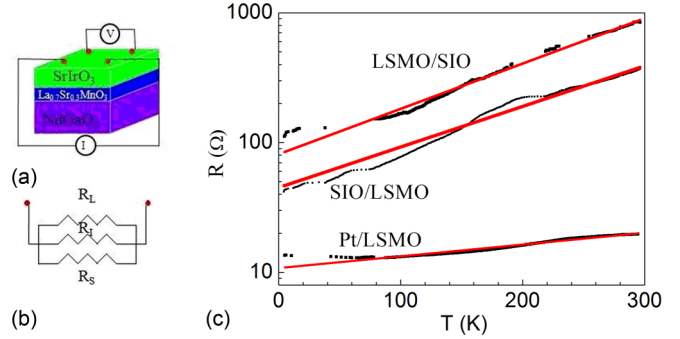
FIG. 3. (a) The circuit for the measurements of the SIO/ LSMO heterostructure resistances (b) Equivalent circuit used for interface resistance R_I calculation. (c) Temperature dependence of R_I for following heterostructures: SIO(10 nm)/LSMO(12 nm), LSMO(15 nm)/SIO(10 nm), and Pt(10 nm)/LSMO(20 nm) are presented in log scale. The thicknesses of the films are indicated in braces.

and [100]SIO‖[100]LSMO‖[001]NGO. Narrow rocking curve (FHMW $= 0.1°$–$0.12°$) for (002)SIO indicates the high quality of the films.

III. DC TRANSPORT OF THE HETEROSTRUCTURE

The electrical properties of films and heterostructure were measured using the four-probe method current-in-plane sheet resistance using Montgomery topology [37] [Fig. 3(a)]. In this case the sheet resistance of the film or the heterostructure is measured. To compare the transport between the films and the heterostructure the temperature-dependent resistance curves are analyzed.

LSMO films exhibit metallic behavior at temperatures below metal-insulator transition temperature of (T_M) which is consistent with previously reported behavior of LSMO epitaxial film on these substrates [34,36]. The maximum resistance in manganite at $T = T_M$ is usually observed near the Curie temperature [36,38]. The temperature-dependent resistance of the SIO film is also reduced with lowering temperature but the reduction is not as significant as that of LSMO films [21,28,39].

To assist in the interpretation of the resistance data, we modeled the resistance (R_H^{1}) of the SIO/LSMO heterostructure as parallel connection of the resistance of the upper layer of the SIO film R_S and the parallel-connected resistances of the bottom LSMO layer $R_L R_H^{1} = R_S R_L/(R_S + R_L)$. It is larger than the measured resistance of the heterostructure (R_H). The presence of the interface resistance connected in series with R_L increased the difference between R_H^{1} and R_H [34,40]. One possible solution is to consider the parallel connected interface resistance R_I as shown in Fig. 3(b). Using obtained sheet resistance of interface SIO/LSMO equal to $R_I = \rho_I/d_S$ we get $\rho_I = 8 \times 10^{-6}\,\Omega$ cm for low temperature $T < 100$ K supposing the thickness of the interface to be equal to 1 nm. We argue that the low specific resistivity of the interface may indicate the existence of a layer of electronic gas with high mobility [1,41]. The temperature dependence of R_I is proportional to $\exp(-AT)$ for the interfaces [see red lines in Fig. 3(c)]. It shows a similar mechanism of current transport in the interfaces [1,41]. The interface resistance for SIO/LSMO

heterostructure differs from the LSMO/SIO heterostructure one, but the coefficient A varies of 0.0072 and 0.008, respectively, within the experimental error 0.0005. The difference in coefficients A is caused by the difference of LSMO film growth on a (110) NGO substrate comparable with LSMO film growth on SIO film. The obtained Pt/LSMO interface has a different temperature dependence of R_I resistance with $A = 0.002$.

Anyway, it is also possible that the effect occurs because the doping of La and Sr or oxygen across the interface or oxygen doping that give additional conductivity is not excluded.

While the electronic properties of the 3d TMO are governed by the strong Coulomb interaction, in the 5d TMO the spin-orbit interaction is a dominating one. It was shown theoretically that in the ballistic regime in a two-layer system consisting of a magnetic insulator and an adjacent nonmagnetic metal the interfacial current appears due to the spin-orbit interaction in the metal layer near the interface [42]. The induced current could have a significant influence on the interface resistance observed in our case [Fig. 3(b)].

The first-principles calculations based on the density-functional theory have been performed in Ref. [43]. It was shown that the charge transfers at the interface from the half-filled spin-orbit entangled $J_{eff} = 1/2$ state of the iridate to the empty $e^{\uparrow g}$ states of iridate. The charge leakage from iridate makes it hole doped, while the manganite side becomes electron doped. The doped carriers make both sides metallic. Approximately the same charge transfer is obtained if one integrates the partial density of states for the Ir and Mn atoms. According to the calculation [43], the charge transfer is 0.06 electrons per interface Ir atom from the iridate to the manganite side. Electron transfer from the Ir to the Ni site, triggering a dramatic electronic and magnetic reconstruction, was observed at the SrIrO$_3$/LaNiO$_3$ interface [44]. The charge transfer across the interface is comparable to the density of the two-dimensional electron gas in the well-studied polar interface of LaAlO$_3$ and SrTiO$_3$ (see, for example, Ref. [45]).

IV. NEUTRON SCATTERING

For the neutron experiment we prepared a heterostructure having properties of neutron magnetic waveguide [46]. This design allows us to get additional sensitivity to the appearance of small magnetic moment in the SIO layer. To make this design we have covered LSMO/SIO structure by a gold layer [see Fig. 4(a)] and increase the thickness of the films in heterostructure. Figure 4(b) shows the hysteresis loops of resulting Au/LSMO/SIO structure measured by SQUID at $T = 300$ K and $T = 100$ K. The paramagnetic signal is increasing rapidly with cooling and leads to the elevated error bar for $T < 100$ K.

The polarized neutron reflectivity (PNR) experiments were conducted on the angle-dispersive reflectometer NREX ($\lambda = 0.428$ nm) at the research reactor FRM-II (Garching, Germany). The polarized neutron beam (with polarization 99.99%) was incident on a sample at grazing angles $\theta = (0.15°–1°)$. The polarization of the reflected beam was analyzed by an analyzer with efficiency 99.2%. In the experiment we applied small external magnetic field $H = 5$ Oe in the plane of the sample and with 5° accuracy along one of the
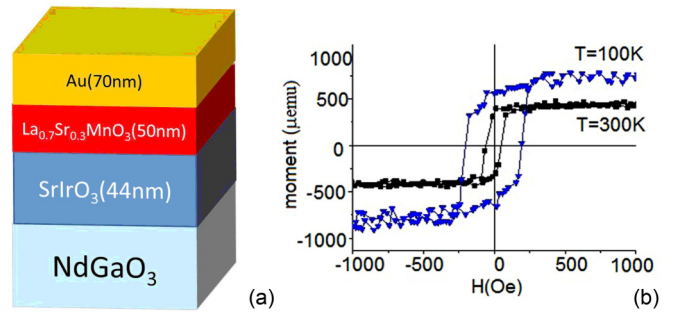
FIG. 4. (a) Sketch of the structure measured by SQUID and neutron-polarized neutron reflectivity. (b) Magnetic hysteresis loops of the heterostructure measured at $T = 300$ K and $T = 100$ K. Background due paramagnetic of the substrate NGO was corrected.

edges of the substrate [Fig. 5(a)]. At a fixed temperature, we measured four reflectivity curves for fixed positions of polarizer and analyzer R^{++}, R^{--}, R^{+-}, and R^{-+} as a function of momentum transfer $Q = 4\pi \sin \theta / \lambda$ [Figs. 5(b) and 5(c)].

On the basics of specular PNR the non-spin-flip reflectivities R^{++}, R^{-} are sensitive to the sum and the difference of the nuclear scattering length density (SLD) profile and the in-plane magnetization component $M_{\parallel} = |M| \cos \alpha$ collinear with the external magnetic field H. Here $|M|$ is the amplitude of the magnetization vector $\boldsymbol{M}$ averaged over all possible microdomains in the plane of the structure and α is the angle between M and $\boldsymbol{H}$. In order to separate magnetic signal from nuclear it is convenient to analyze spin asymmetry $S \equiv (R^{++} - R^{--})/(R^{++} + R^{--})$ which is proportional to $M_{\parallel}$. The spin-flip (SF) reflectivities R^{+-}, R^{-+} in turn are sensitive to square of noncollinear to H in-plane component of magnetization $M_{\perp} = |M| \sin \alpha$. In the majority of PNR experiments, including ours, $R^{+-}(Q) = R^{-+}(Q)$. In this regard, for analysis we averaged spin-flip reflectivity $R^{SF} \equiv [R^{+-} + R^{-+}]/2$ to improve statistical accuracy [46–50].

Figures 5(b) and 5(c) show the PNR data measured at $T = 275$ K and $T = 3$ K, correspondingly. We observed strong SF scattering with the resonance peak in the vicinity of critical momentum transfer $Q_{cr} = 0.16$ nm^{-1} having intensity of $R^{SF}(Q_{WG}) = 12\%$ [arrow in Fig. 5(b)]. At the same time, we observed nonzero spin asymmetry with maximum of $S = -20\%$ slightly above Q_{cr}. These curves can be fitted with the nuclear SLD profile depicted in the inset to Fig. 6(c) and averaged LSMO magnetic moment that changed with reduced temperature. At $T = 300$ K it is equal to 2 μ_B/Mn tilted on the angle on angle $\alpha = 38°$ to the direction of external field.

Figure 6(a) shows that suppression of integrated spin-flip scattering (SF) and the increase of the averaged spin asymmetry (SA) take place systematically below 150 K. After cooling of the sample down to 3 K we observed 3 times decreased intensity of SF scattering accompanied by a 2 times increased SA [Fig. 6(a)]. This behavior can naturally be explained by the turn of magnetization vector of LSMO closer to the external field. The temperature dependence of the saturation moment is well fitted within the mean-field theory with bulk Curie temperature $T_m = 340$ K [Fig. 6(b)] [51]. Quantitatively we can describe the data at 3 K by LSMO averaged magnetic moment 3.7 μ_B/Mn turned at $\alpha = 26°$. We note that the average
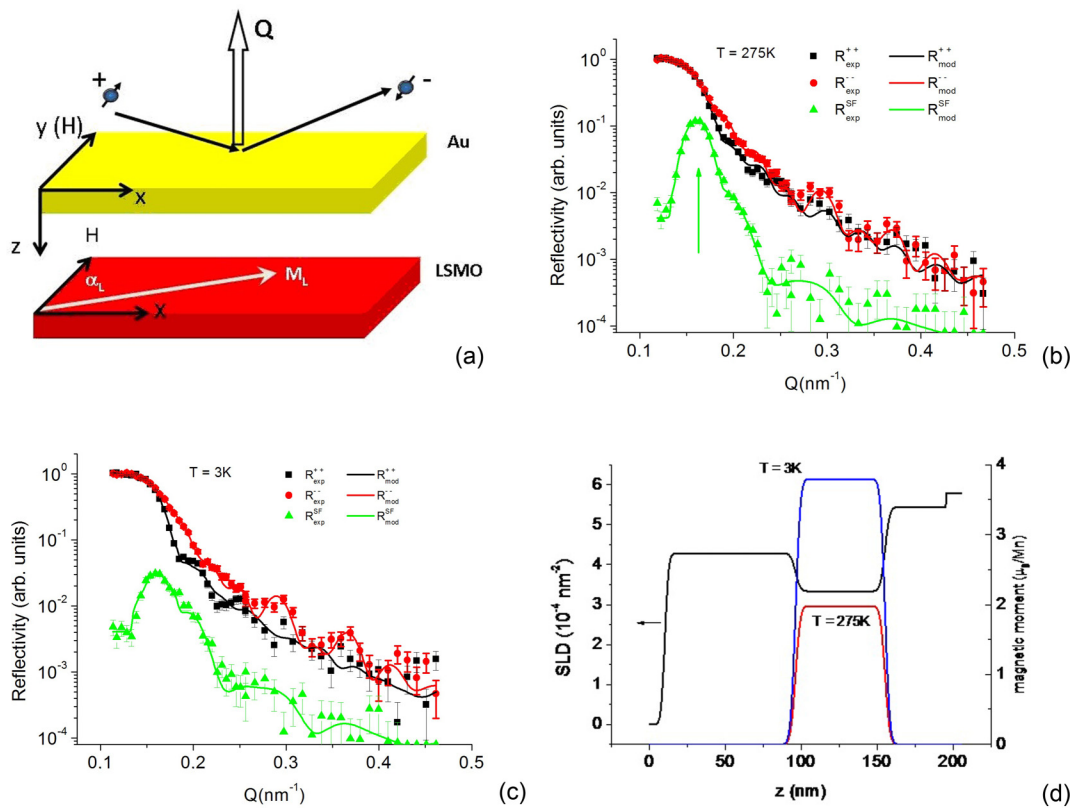
FIG. 5. (a) Topology of neutron experiment. α is the angle between the magnetization direction of LSMO film and external magnetic field. Experimental (dots) and model (lines) polarized neutron reflectivity measured at (b) $T = 275$ K, (c) $T = 3$ K. Arrow indicates the critical angle. (d) Depth profiles of nuclear SLD at $T = 275$ K and magnetic moment both at $T = 275$ K and $T = 3$ K.

magnetic moment obtained from neutron data at remanence at low temperature is close to the saturation moment obtained from the SQUID. This correspondence between neutron and SQUID data gives us reason to believe that at low temperature and low field the magnetic state of LSMO is close to the single domain.

We also tried another model at which magnetization of LSMO was fixed to $3.7\,\mu_B$/Mn and magnetization of SIO varied. Since the whole structure was designed as a magnetic waveguide sensitive to the appearance of magnetic moment in SIO, we indeed can describe suppression of the SF peak by small positive magnetization (10% of LSMO moment) in the whole SIO layer. However, such small distortion of the magnetic contrast cannot describe increase of spin asymmetry. On the other hand, the presence of the magnetic moment at the interface SIO/LSMO layer ($\sim$1-nm thickness) is beyond sensitivity of PNR. Note, PNR experiment allows one to obtain both amplitude of magnetization vector $|M|$ and angle of its
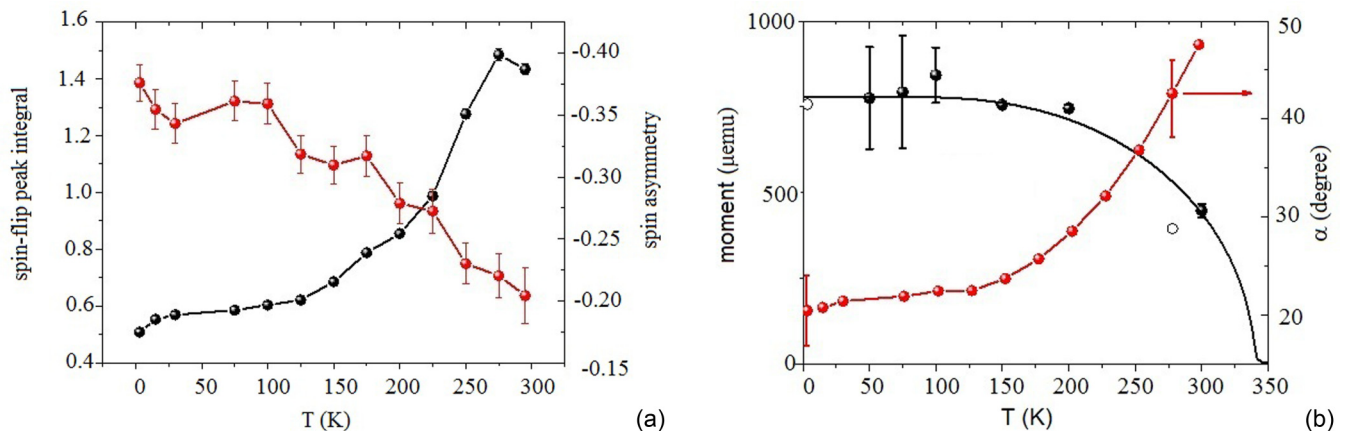
FIG. 6. (a) Temperature dependence of integrated spin-flip scattering (black circles) and averaged spin asymmetry (red circles). (b) Saturation magnetization versus temperature measured by SQUID (black circles) and mean-field approximation with Curie temperature $T_{CU} = 340$ K (solid line). The neutron data are also shown on the curve (open circles).
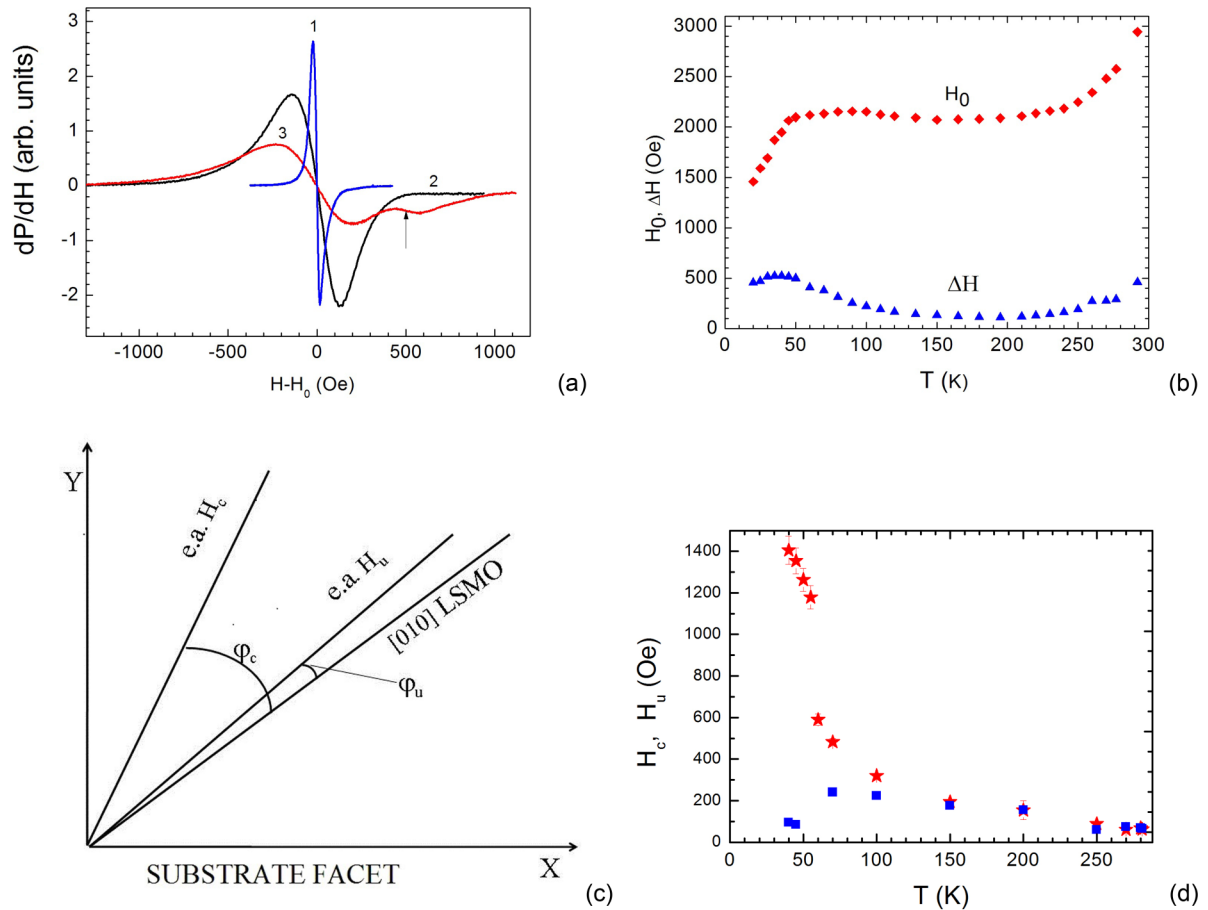
FIG. 7. (a) Ferromagnetic resonance spectra $dP/dH(H)$ for LSMO film and SIO/LSMO heterostructures: (1) 15-nm-thick LSMO film at $T = 300$ K, (2) SIO/LSMO heterostructure with 12-nm thicknesses of LSMO and 10 nm SIO, T = 90 K and (3) $T = 40$ K. "New" line on FMR spectrum is indicated by arrow. (b) Temperature dependences of resonance field H_0 and linewidth ΔH for heterostructure SIO/LSMO. (c) Easy axes H_c and H_u at room temperature related to the substrate facets. (d) Temperature dependence of biaxial magnetic anisotropy H_c (red stars) and uniaxial magnetic anisotropy H_u (filled squares) for the heterostructure.

inclination to the external field for any magnetic field applied starting from small values as ~3–5 Oe to the maximum which the magnet can produce. This is in contrast to SQUID, which measures only collinear component of magnetic moment on external field.

The density-functional results [43] show that a charge transfer at the interface from the iridate to the manganite side discussed in Sec. III of the paper is the main reason for the ferromagnetic interaction in the iridate/manganite heterostructure. The electrons transferred to the manganite add ferromagnetic ordering through the double-exchange interaction, while the iridate part becomes ferromagnetic due to the doping of the half-filled Mott-Hubbard insulator [15,17,31]. The occurrence of magnetism at the interface caused by hybridization of Mn and Ir orbitals is the reason for the axis of easy magnetization rotation between the crystallographic directions: (110) $La_{0.7}Sr_{0.3}MnO_3$ and (001) $La_{0.7}Sr_{0.3}MnO_3$ in manganite/iridate superlattice [15,31].

Thus we observed turn of magnetic vector at remanence on 26° in PNR experiment [Fig. 6(b)]. Similar turn of easy-axis direction was observed recently in $LaNiO_3/DyScO_3$ superlattice [52] and it was explained by appearance of a magnetic moment at Dy with strong anisotropy noncollinear to the easy

axis of nickelate. Strong exchange interaction of Ni and Dy atoms at the interface leads to the turn of magnetic moment in nickelate towards easy axis of $DyScO_3$ layer.

V. MAGNETIC ANISOTROPY IN HETEROSTRUCTURE

To record the magnetic resonance spectra, we used the Bruker ER 200 spectrometer operating in the X band ($f =$ 9.6 GHz) with the Oxford ESR 900 cryo-insert. In all FMR experiments the external magnetic field was in the plane of the substrate (110)NGO and the magnetic component of the microwave field was directed along the normal to the substrate [53]. All spectra were recorded in substrates with dimensions 2.5×2.5 mm^2 with thickness of 10 and 4 nm for SIO and LSMO, accordingly. It should be noted that the thickness of both LSMO and SIO were four times less than that of heterostructure in the neutron experiment and that the LSMO film is a bottom layer.

Figure 7(a) shows the FMR spectra dP/dH here P is a reflection value) of an autonomous LSMO film at $T = 300$ K and for heterostructures: SIO/LSMO at two temperatures, T = 90 and 40 K. Note that at room temperature only the FMR line from the LSMO layer is observed, since the sensitivity

of the spectrometer does not allow recording the absorption spectrum from the paramagnetic SIO layer. It can be seen from Fig. 7(a) that deposition of a SIO layer broadens the FMR line. The observed broadening can be caused by additional channels of magnetization relaxation due to the leakage of magnetization across the SIO/LSMO interface due to the spin current.

Figure 7(b) shows the resonance field H_0 and linewidth of FMR spectrum for the heterostructure structures measured under the condition that the external magnetic field was directed along the hard axis of the uniaxial magnetic anisotropy. The dependence on the temperature obtained characterizes the change in the magnetization of the heterostructure [53]. A sharp decrease in the H_0 value in the heterostructure is observed with a decrease in temperature below 50 K. Such a decrease cannot be explained by a sharp increase in the LSMO film magnetization. As a rule, with a decreasing temperature, the dependence H_0 (T) for LSMO films saturates at temperatures below 100 K [53].

LSMO films grown on NGO substrates exhibit an induced uniaxial planar anisotropy reaching hundreds of Oe at room temperature in addition to the inherent biaxial one to the cubic structure of LSMO film [53–56]. To determine the magnetic anisotropy of the heterostructure, the angular dependencies of the FMR spectrum at fixed temperatures were recorded (see the Appendix). H_0 is a function of the magnitude of the equilibrium magnetization M_0 and anisotropy fields $H_u = 2K_u/M_0$ and $H_c = 2K_c/M_0$, where K_u and K_c are the uniaxial and the biaxial cubic anisotropy constants, correspondingly.

The directions of easy axis for the uniaxial and the biaxial cubic anisotropy are determined by φ_u and φ_c angles, correspondingly [Fig. 7(c)]. φ_u is close to the direction of the [010]LSMO film, while φ_c of biaxial cubic anisotropy forms the angle 45° with φ_u.

Figure 7(d) shows the temperature dependence of the uniaxial H_u and biaxial magnetic anisotropy H_c for SIO/LSMO heterostructure. At room temperature, H_u dominates or equal over H_c. As the temperature decreases, H_u and H_c increase slowly until $T \approx 100$ K as in heterostructures manganites with 3d oxides [54–57]. In SIO/LSMO heterostructures there is a significant increase in H_c (T) at $T < 100$ K, which is absent upon the contact of 3d oxides [56]. A similar increase in the magnetization of the LSMO layer has been observed at temperatures below 150 K in LSMO/SrRuO₃ heterostructure. It was interpreted as the appearance of interlayer exchange interaction with the SrRuO₃ layer passed into ferromagnetic state with $T_{CU} = 150$ K [56]. The increase in H_c associated with H_u leads to the turning of the heterostructure SIO/LSMO total magnetization vector that was observed in the neutron experiment (see Sec. IV).

In the temperature range where a sharp increase in H_c (T) is observed at $T < 100$ K [see Fig. 7(d)] an additional FMR line appeared which indicates the appearance of an additional ordered ferromagnetic state in the heterostructure. Signs of ferromagnetism at the SIO/LSMO interface were recorded in Refs. [16,32,55,57]. The emergence of a "new" FMR line can be caused by the appearance of a ferromagnetic order at SIO/LSMO interface film, as observed in the SIO/LSMO [15] superlattice and predicted theoretically in Ref. [43]. The transferred charge (see Sec. II) plays an important role

in altering the magnetic interactions near the interface. The density-functional results [43] show that the interfacial magnetism is controlled by a net charge transfer at the interface from the SIO to the manganite. The doped electrons turn the manganite part metallic and change ferromagnetic states via the double-exchange mechanism. The hole-doped iridate part, on the other hand, behaves like a half-filled Mott-Hubbard insulator and becomes ferromagnetic [43]. The emergence of ferromagnetism at the interface of the 3d manganite and 5d iridate interface is in agreement with the experimental observation [16] and unravel its mechanism.

VI. SPIN CURRENT

It was theoretically shown [58] (see also Refs. [59,60]) that in the bilayers ferromagnet/normal metal the pure spin current j_s is formed by a spin injection from ferromagnet to normal metal. The density of the pure spin current entering at the interface is given by the equation

$$j_S = \frac{\hbar}{8\pi}\mathrm{Re}(g^{\uparrow\downarrow})\left[\mathbf{m} \times \frac{\partial \mathbf{m}}{\partial t}\right], \qquad (1)$$

where $g^{\uparrow\downarrow}$ is spin-mixing conductance of interface, **m** is magnetic moment precessing under external microwave external radiation. The imaginary part of the spin-mixing conductance is significantly less than the real part (see Refs. [61,62]). Therefore, we can consider only the real part the spin-mixing conductance.

To estimate the real part of the spin-mixing conductance we use the fact that during FMR there is an additional spin relaxation generated by the spin current in the ferromagnetic/normal metal structure FMR [59,63–65]. Thus, the spin-mixing conductance can be expressed through the widening of the FMR spectrum line of the heterostructure SIO/LSMO compared with LSMO film FMR spectrum [see Fig. 7(a)] [59,63–65].

$$g^{\uparrow\downarrow} = \frac{4\pi\gamma_g M_s t_{\mathrm{LSMO}}}{g\mu_\beta\omega_f}(\Delta H_{\mathrm{SIO/LSMO}} - \Delta H_{\mathrm{LSMO}}), \qquad (2)$$

where the magnetization LSMO film $M_s = 300$ Oe, the thickness for LSMO film $t_{\mathrm{LSMO}} = 12$ nm, $\mu_B = 9.274 \times 10^{-21}$ erg/G, $g = 2$, $\gamma_g = 17.605 \times 10^6\,\mathrm{s}^{-1}\,\mathrm{G}^{-1}$, $\omega_f = 2\pi \times 9.51 \times 10^9\,\mathrm{s}^{-1}$ is the microwave angular frequency in our case. We got $\Delta H_{\mathrm{SIO/LSMO}} - \Delta H_{\mathrm{LSMO}} = 20$ Oe from experimental data and $g_{\mathrm{eff}}^{\uparrow\downarrow} = 0.95 \times 10^{18}\,\mathrm{m}^{-2}$ at $T = 300$ K. It could be compared with $g^{\uparrow\downarrow}$ for interfaces $\mathrm{SrRuO_3}/\mathrm{La_{2/3}Sr_{1/3}MnO_3}$, $\mathrm{Pt}/\mathrm{Ni_{80}Fe_{20}}$, Pt/YIG (YIG is yttrium iron garnet) and SIO/LSMO $5 \times 10^{18}\,\mathrm{m}^{-2}$ [66], $2.1 \times 10^{19}\,\mathrm{m}^{-2}$ [59], $4.8 \times 10^{20}\,\mathrm{m}^{-2}$ [63], and $1.2 \times 10^{18}\,\mathrm{m}^{-2}$ [35], correspondingly.

The spin current can be detected using the inverse spin Hall effect (ISHE) which is observed in materials with the strong spin-orbit interaction [67,68]. The charge current arising due to ISHE j_Q is given by

$$\vec{j}_Q = \theta_{\mathrm{SH}}\frac{e}{\hbar}[\vec{n} \times \vec{j}_s], \qquad (3)$$

where the relation between spin and charge currents is determined by the dimensionless spin Hall angle θ_{SH}, and $\vec{n}$ is a unit vector in the direction of the spin momentum flow.
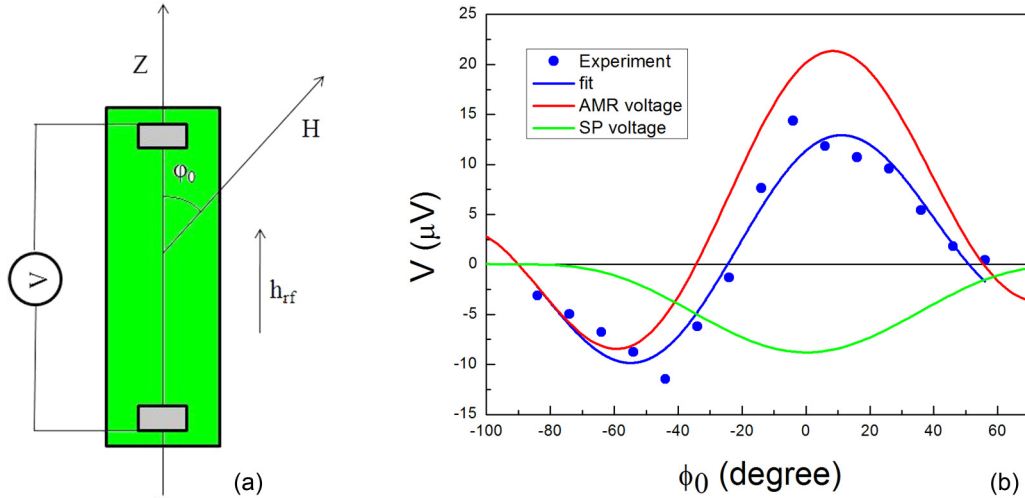
FIG. 8. (a) Topology for angular spin-voltage measurements. ϕ_0 is angle between current direction (Z) and $\psi = -22°$ is the angle between easy axes of the manganite and Z direction. ψ is not shown in (a). (b) Angular dependence of voltage $V(\phi)$ arising in the SIO/LSMO heterostructure. The red line represents symmetric part of the AMR signal V^{AMR} and the green line represents signal from the spin pumping V_Q. Solid blue line is the sum of two contributions [see Eq. (4)].

The results on spin pumping in the heterostructure SIO/LSMO deposited on NGO substrate are shown below. The sample had the form of a strip with electric silver contacts at the edges for the voltage measurements [see Fig. 8(a)]. It was placed in the central plane of the rectangular TE_{012} microwave cavity. Microwave pumping was produced from Gunn diode with output up to 75 mW at the frequency $\omega_f/2\pi = 9.0$ GHz. Microwave power is modulated at the frequency $f_M = 100$ kHz. Similarly, the voltage $V(H)$ was lock-in amplified and detected with the reference frequency f_M. The enhancement of the sensitivity was distinguished by accumulation of the voltage signal at repeated magnetic-field sweeping across the FMR line. To rule out the parasitic contribution that is constant for the opposite orientations of the magnetic field, we use the difference for the signals with opposite orientations of the magnetic field.

We also considered the dc voltage arising due to the presence of anisotropic magnetoresistance (AMR) in LSMO film [69–71]. Consequently the balance of the full dc voltage and the angle-dependent spin voltage should be written as a combination of symmetric Lorentzian function of spin voltage and two components, an antisymmetric and symmetric Lorentzian function of AMR signals [69–71]. An external magnetic field H was rotated in the plane of the substrate to separate the spin-pump signal from AMR signal [see Fig. 8(a)]. In our geometry the angular dependences of the detected voltage V, the contribution of the spin pumping V_Q, and AMR voltage V^{AMR} contributions are given by the following equation (for the detailed description see Ref. [71]):

$$V(\phi_0) = V^{\mathrm{AMR}} \sin 2(\phi_0 - \psi) \sin\phi + V_Q \sin^3\phi_0, \quad (4)$$

where ϕ_0 is the angle between the external magnetic field and the direction of the current measured and ψ is the angle between the easy axes of the manganite and the direction of the current. By rotating the external field H in the plane of substrate we measure the voltage for angles in the range $180°$ in increments of $10°$. Note that there is a special AMR mechanism whose effect depends on the direction of the easy

axis and does not depend on the direction of the electric current (see Ref. [71]). The easy axes were determined using a commercial X-range electron paramagnetic resonance spectrometer Bruker ER 200. Selecting the angular dependence using Eq. (4), we obtain the following relationship between the symmetric anisotropic magnetoresistance signal and the amplitude of spin-pumping signal: $V_Q/V^{\mathrm{AMR}} = 0.23 \pm 0.03$ (see also Fig. 4 [70]).

Experimental value of spin voltage V_Q is equal to $8.8\,\mu$V, that order of value equal to the voltage that is given by the equation [59,65]

$$V_Q = -\frac{\Theta_{\mathrm{SH}} eLP\omega_f \lambda_{sd} g^{\uparrow\downarrow}}{2\pi(\sigma_{\mathrm{LSMO}} t_{\mathrm{LSMO}} + \sigma_{\mathrm{SIO}} t_{\mathrm{SIO}})} \left(\frac{h_{rf}}{2\Delta H}\right)^2, \quad (5)$$

where we have considered the case $t_{\mathrm{SIO}} \gg \lambda_{sd}$. The half-width of the FMR line for heterostructure is $\Delta H = \Delta H_{\mathrm{SIO/LSMO}} = 18$ Oe is the half-width of the FMR line for heterostructure, $g^{\uparrow\downarrow} = 0.95 \times 10^{18}\,\mathrm{m}^{-2}$, $L = 4$ mm is the distance between contacts, $t_{\mathrm{SIO}} = 10$ nm and $t_{\mathrm{LSMO}} = 30$ nm are the thicknesses of the iridate and manganite, respectively, $h_{rf} = 0.1$ Oe is the amplitude of microwave magnetic field, $\sigma_{\mathrm{LSMO}} = 10^3\,\Omega^{-1}\,\mathrm{cm}^{-1}$ and $\sigma_{\mathrm{SIO}} = 3 \times 10^3\,\Omega^{-1}\,\mathrm{cm}^{-1}$ is the charge conductivity of manganite and iridate, correspondingly, $P = 1.3$ is the ellipticity corrector factor [72]. Use the above values and Eq. (5) to find a product $\Theta_{SH}\lambda_{sd} \approx 1.4$ that is consistent with results in Refs. [35,73–75].

VII. CONCLUSION

Measurements of the dc transport and the magnetic properties of $\mathrm{SrIrO_3/La_{0.7}Sr_{0.3}MnO_3}$ epitaxial heterostructures showed the presence of unusual properties of the interface between the materials. The dc measurement shows the presence of a conduction channel at the iridate/manganite interface. The magnetization and magnetic profiles of SIO/LSMO heterostructure was investigated by SQUID and neutron scattering. The spin-mixing conductance was determined by comparing FMR linewidth for the LSMO film and iridate

TABLE I. Magnetic parameters of the heterostructure SIO/LSMO, obtained from angle dependence of resonance field.

T, K	M_0, Oe	H_u, Oe	H_c, Oe	φ_u, grad	φ_c, grad
150	309.5 ± 0.6	165 ± 3	105 ± 3	1.2 ± 0.6	44.9 ± 0.5
90	277 ± 2	200 ± 8	199 ± 9	1 ± 1.3	45.1 ± 0.7
40	260 ± 3	215 ± 17	325 ± 19	2 ± 2.5	44.0 ± 0.9

heterostructure with SIO on top of LSMO film. At the temperatures below 60 K a sharp increase in biaxial anisotropy was observed and an additional FMR line emerged, indicating the occurrence of an additional ordered ferromagnetic state in the heterostructure. One of the possible reasons may be the appearance of ferromagnetism at the interface SIO/LSMO. Neutron-scattering data can be explained by rotating the magnetization vector of the heterostructure on $26°$ close to the external field. We have measured the dc voltage on the SIO film caused by spin pumping and by the anisotropic magnetoresistance in the heterostructure in the presence of FMR in the heterostructure.

APPENDIX

The method for determining the parameters of the magnetic anisotropy consisted of processing the angular dependences of the resonant fields of the FMR spectra. The solution of the linearized Landau-Lifshitz-Gilbert equation is used for the evolution of the magnetization M_0 in an external constant magnetic field H under the action of the magnetic component of the radio-frequency field. This solution gives an analytic connection between the external resonance field H_0 and the frequency ω under FMR conditions [53,76]:

$$\left(\frac{\omega}{\gamma}\right)^2 = \left(4\pi M_0 + H_0(\phi) + H_u\cos^2\phi_u + H_c\frac{1+\cos^2 2\phi_c}{2}\right)$$
$$\times \ (H_0 + H_u\cos 2\phi_u + H_c\cos 4\phi_c). \tag{A1}$$
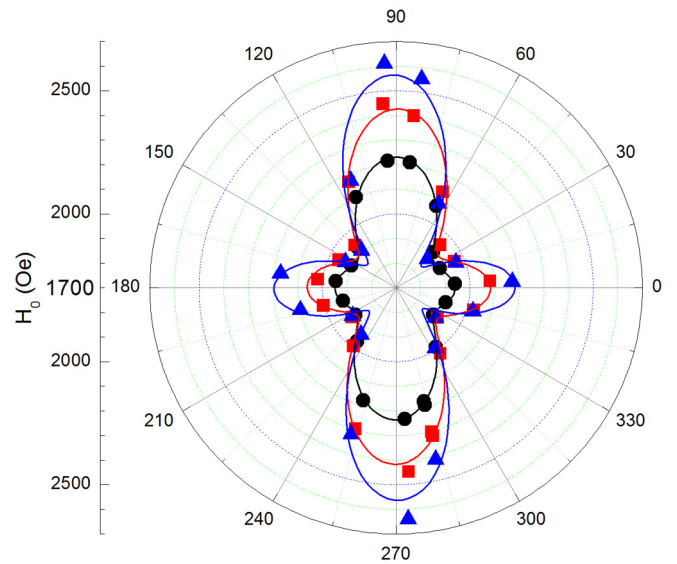
FIG. 9. Angular dependences of the resonance field for the SIO/LSMO heterostructure obtained at temperatures: $T = 150\,\text{K}$ (filled circles), $T = 90\,\text{K}$ (red squares), $T = 40\,\text{K}$ (blue triangles). Color solid lines are the fitting according to formula (1) with the parameters indicated in Table I.

Here γ is the gyromagnetic ratio, M_0 is the equilibrium magnetization, $H_u = 2K_u/M_0$, $H_c = 2K_c/M_0$, K_u is the uniaxial anisotropy constant, and K_c is the biaxial cubic anisotropy constant. As a result, the values of K_u, K_c, M_0, as well as the angles between the easy axis of the uniaxial anisotropy and the external magnetic field φ_u and between the easy axis of the biaxial cubic anisotropy and the external magnetic field φ_c are determined from the angular dependence of the magnitude of the resonant magnetic field H_0. Both easy axes lie in the plane of the substrate.

Figure 9 shows the $H_0(\varphi)$ for the SIO/LSMO heterostructure at room temperature. The external magnetic field is rotated around the normal to the film plane by an angle φ. The angle was measured from the direction of [010]LSMO. The external magnetic field and the magnetic component of the microwave field were in the plane of the film. The change of resonant field with the angle is due to the planar magnetic anisotropy of the SIO/LSMO heterostructure. The angular dependence was described by a resonance relation (A1) taking into account magnetic uniaxial and cubic plane anisotropies [53].

[1] Y. Tokura, Phys. Today **56**(7), 50 (2003).

[2] E. Dagotto, Science **309**, 257 (2005).

[3] S. J. Moon, H. Jin, K. W. Kim, W. S. Choi, Y. S. Lee, J. Yu, G. Cao, A. Sumi, H. Funakubo, C. Bernhard, and T. W. Noh, Phys. Rev. Lett. **101**, 226402 (2008).

[4] D. Pesin and L. Balents, Nat. Phys. **6**, 376 (2010).

[5] W. Witczak-Krempa, G. Chen, Y. B. Kim, and L. Balents, Annu. Rev. Condens. Matter. Phys. **5**, 57 (2014).

[6] R. Schaffer, E. Lee, B. Yang, and Y. Kim, Rep. Prog. Phys. **79**, 094504 (2016).

[7] A. Shitade, H. Katsura, J. Kuneš, X.-L. Qi, S.-C. Zhang, and N. Nagaosa, Phys. Rev. Lett. **102**, 256403 (2009).

[8] D. Xiao, W. Zhu, Y. Ran, N. Nagaosa, and S. Okamoto, Nat. Commun. **2**, 596 (2011).

[9] F. Wang and Y. Ran, Phys. Rev. B **84**, 241103(R) (2011).

[10] X. Wan, A. M. Turner, A. Vishwanath, and S. Y. Savrasov, Phys. Rev. B **83**, 205101 (2011).

[11] J. G. Kim, D. Casa, M. H. Upton, T. Gog, Y.-J. Kim, J. F. Mitchell, M. van Veenendaal, M. Daghofer, J. van den Brink, G. Khaliullin, and B. J. Kim, Phys. Rev. Lett. **108**, 177003 (2012).

[12] Y. K. Kim, N. H. Sung, J. D. Denlinger, and B. J. Kim, Nat. Phys. **12**, 37 (2016).

[13] I. Fina, X. Marti, D. Yi, J. Liu, J. H. Chu, C. Rayan-Serrao, S. Suresha, A. B. Shick, J. Z̆elezny, T. Jungwirth, J. Fontcuberta, and R. Ramesh, Nat. Commun. **5**, 4671 (2014).

[14] J. Matsuno, K. Ihara, S. Yamamura, H. Wadati, K. Ishii, V. V. Shankar, H.-Y. Kee, and H. Takagi, Phys. Rev. Lett. **114**, 247209 (2015); J. Matsuno, N. Ogawa, K. Yasuda, F. Kagawa, W. Koshibae, N. Nagaosa, Y. Tokura, and M. Kawasaki, Sci. Adv. **2**, e1600304 (2016).

[15] D. Yi, J. Liu, S.-L. Hsu, L. Zhang, Y. Choi, J.-W. Kim, Z. Chen, J. D. Clarkson, C. R. Serrao, E. Arenholz, P. J. Ryan, H. Xu, R. J. Birgeneau, and R. Ramesh, Proc. Natl. Acad. Sci. U.S.A. **113**, 6397 (2016).

[16] J. Nichols, X. Gao, S. Lee, T. L. Meyer, J. W. Freeland, V. Lauter, D. Yi, J. Liu, D. Haskel, J. R. Petrie, E.-J. Guo, A. Herklotz, D. Lee, T. Z. Ward, G. Eres, M. R. Fitzsimmons, and H. N. Lee, Nat. Commun. **7**, 12721 (2016).

[17] S. Okamoto, J. Nichols, C. Sohn, S. Y. Kim, T. W. Noh, and H. N. Lee, Nano Lett. **17**, 2126 (2017).

[18] R. Chaurasia, K. C. Kharkwal, and A. K. Pramanik, Phys. Lett. A **383**, 1642 (2019).

[19] J. M. Longo, J. A. Kafalas, and R. J. Arnott, J. Solid State Chem. **3**, 174 (1971).

[20] F.-X. Wu, Z. Jian, L. Y. Zhang, Y. B. Chen, Z. Shan-Tao, G. Zheng-Bin, Y. Shu-HuaY, and C. Fan-Feng, J. Phys.: Condens. Matter **25**, 125604 (2013).

[21] A. Biswas and Y. H. Jeong, Curr. Appl Phys. **17**, 605 (2017).

[22] L. Zhang, Q. Liang, Y. Xiong, B. Zhang, L. Gao, H. Li, Y. B. Chen, J. Zhou, S.-T. Zhang, Z.-B. Gu, S.-h. Yao, Z. Wang, Y. Lin, and Y.-F. Chen, Phys. Rev. B **91**, 035110 (2015).

[23] Y. F. Nie, P. D. C. King, C. H. Kim, M. Uchida, H. I. Wei, B. D. Faeth, J. P. Ruf, J. P. C. Ru, L. Xie, X. Pan, C. J. Fennie, D. G. Schlom, and K. M. Shen, Phys. Rev. Lett. **114**, 016401 (2015).

[24] L. Zhang, B. Pang, Y. B. Chen, and Y. Chen, Crit. Rev. Solid State Mater. Sci. **43**, 367 (2018).

[25] Y. Liu, H. Masumoto, and T. Goto, Mater. Trans. **46**, 100 (2005).

[26] L. Fruchter, O. Schneegans, and Z. Z. Li, J. Appl. Phys. **120**, 075307 (2016).

[27] J. H. Gruenewald, J. Nichols, J. Terzic, G. Cao, J. W. Brill, and S. S. A. Seo, J. Mater. Res. **29**, 2491 (2014).

[28] Y.V. Kislinskii, G. A. Ovsyannikov, A. M. Petrzhik, K. Y. Constatinian, N. V. Andreev, and T. A. Sviridova, Phys. Solid State **57**, 2519 (2015).

[29] B. J. Kim, H. Jin, S. J. Moon, J.-Y. Kim, B.-G. Park, C. S. Leem, J. Yu, T. W. Noh, C. Kim, S.-J. Oh, J.-H. Park, V. Durairaj, G. Cao, and E. Rotenberg, Phys. Rev. Lett. **101**, 076402 (2008).

[30] J. G. Zhao, L. X. Yang, Y. Yu, F. Y. Li, R. C. Yu, Z. Fang, L. C. Chen, and C. Q. Jin, J. Appl. Phys. **103**, 103706 (2008).

[31] D. Yi, C. L. Flint, P. P. Balakrishnan, K. Mahalingam, B. Urwin, A. Vailionis, A. T. N'Diaye, P. Shafer, E. Arenholz, Y. Choi, K. H. Stone, J.-H. Chu, B. M. Howe, J. Liu, I. R. Fisher, and Y. Suzuki, Phys. Rev. Lett. **119**, 077201 (2017).

[32] D. Meyers, Y. Cao, G. Fabbris, N. J. Robinson, L. Hao, C. Frederick, N. Traynor, J. Yang, J. Lin, M. H. Upton, D. Casa, J.-W. Kim, T. Gog, E. Karapetrova, Y. Choi, D. Haskel, P. J. Ryan, L. Horak, X. Liu, J. Liu, and M. P. M. Dean, Sci. Rep. **9**, 4263 (2019).

[33] T. Yu, B. Deng, L. Zhou, P. Chen, Q. Liu, X. Ning, J. Zhou, Z. Bian, Z. Luo, C. Qiu, X. Shi, and H., and He, ACS Appl. Mater. Interfaces **11**, 44837 (2019).

[34] T. A. Shaikhulov, G. A. Ovsyannikov, V. V. Demidov, and N. V. Andreev, J. Exp. Theor. Phys. **129**, 112 (2019).

[35] S. Crossley, A. G. Swartz, K. Nishio, Y. Hikita, and H. Y. Hwang, Phys. Rev. B **100**, 115163 (2019).

[36] G. A. Ovsyannikov, A. M. Petrzhik, I.. Borisenko, A. A. Klimov, Yu. A. Ignatov, V. V. Demidov, and S. A. Nikitov, J. Exp. Theor. Phys. **108**, 48 (2009).

[37] H. C. Montgomery, J. Appl. Phys. **42**, 2971 (1971).

[38] A. Urushibara, Y. Moritomo, T. Arima, A. Asamitsu, G. Kido, and Y. Tokura, Phys. Rev. B **51**, 14103 (1995).

[39] E. J. Moon, A. F. May, P. Shafer, E. Arenholz, and S. J. May, Phys. Rev. B **95**, 155135 (2017).

[40] C. T. Boone, J. M. Shaw, H. T. Nembach, and T. J. Silva, J. Appl. Phys. **117**, 223910 (2015).

[41] S. Thiel, G. Hammer, A. Schmehl, C. W. Schneider, and J. Mannhart, Science **313**, 1942 (2006).

[42] M. Ye. Zhuravlev, A. V. Vedyayev, M. S. Titova, N. V. Ryzhanova, and D. Gusakova, J. Magn. Magn. Mater. **441**, 572 (2017).

[43] S. Bhowal and S. Satpathy, AIP Conf. Proc. **2005**, 020007 (2018); Phys. Rev. B **99**, 245145 (2019).

[44] X. Liua, M. Kotiugaa, H.-S. Kima, A. T. N'Diayeb, Y. Choi, Q. Zhang, Y. Cao, M. Kareev, F. Wen, B. Pal, J. W. Freeland, L. Gu, D. Haskel, P. Shafer, E. Arenholz, K. Haule, D. Vanderbilt, K. M. Rabe, and J. Chakhalian, Proc. Natl. Acad. Sci. U.S.A. **116**, 19863 (2019).

[45] A. Ohtomo and H. Hwang, Nature (London) **427**, 423 (2004).

[46] Y. N. Khaydukov, B. Nagy, J.-H. Kim, T. Keller, A. Ruhm, Yu. V. Nikitenko, K. N. Zherenkov, J. Stahn, L. F. Kiss, A. Csik, L. Bottyan, and A. L. Aksenov, J. Exp. Theor. Phys. Lett. **98**, 107 (2013).

[47] H. Zabel, K. Theis Brohl, and B. P. Toperverg, *Handbook of Magnetism and Advanced Magnetic Materials* (John Wiley & Sons, New York, 2007).

[48] Yu. N. Khaydukov, G. A. Ovsyannikov, A. E. Sheyerman, K. Y. Constantinian, L. Mustafa, T. Keller, M. A. Uribe-Laverde, Yu. V. Kislinskii, A. V. Shadrin, A. Kalaboukhov, B. Keimer, and D. Winkler, Phys. Rev. B **90**, 035130 (2014).

[49] Yu. Khaydukov, A. M. Petrzhik, I. V. Borisenko, A. Kalabukhov, D. Winkler, T. Keller, G. A. Ovsyannikov, and B. Keimer, Phys. Rev. B **96**, 165414 (2017).

[50] Yu. Khaydukov and Yu. N. Nikitenko, Nucl. Instrum. Methods Phys. Res., Sect. A **629**, 245 (2011).

[51] C. Kittel, *Introduction to Solid State Physics*, 7th ed. (Wiley, New York, 1996), 7th ed.

[52] M. Bluschke, A. Frano, E. Schierle, M. Minola, M. Hepting, G. Christiani, G. Logvenov, E. Weschke, E. Benckiser, and B. Keimer, Phys. Rev. Lett. **118**, 207203 (2017).

[53] V. V. Demidov, I. V. Borisenko, A. A. Klimov, G. A. Ovsyannikov, A. M. Petrzhik, and S. A. Nikitov, J. Exp. Theor. Phys. **112**, 825 (2011).

[54] Y. Moritomo, A. Asamitsu, and Y. Tokura, Phys. Rev. B **51**, 16491 (1995).

[55] V. V. Demidov, G. A. Ovsyannikov, A. M. Petrzhik, I. V. Borisenko, A. V. Shadrin, and R. Gunnarsson, J. Appl. Phys. **113**, 163909 (2013).

[56] V. V. Demidov and G. A. Ovsyannikov, J. Appl. Phys. **122**, 013902 (2017).

[57] V. V. Demidov, N. V. Andreev, T. A. Shaikhulov, and G. A. Ovsyannikov, J. Magn. Magn. Mater. **497**, 165979 (2020).

[58] Y. Tserkovnyak, A. Brataas, and G. E. W. Bauer, Phys. Rev. Lett. **88**, 117601 (2002).

[59] O. Mosendz, V. Vlaminck, J. E. Pearson, F. Y. Fradin, G. E. W. Bauer, S. D. Bader, and A. Hoffmann, Phys. Rev. B **82**, 214403 (2010).

[60] Y. Wang, R. Ramaswamy, and H. Yang, J. Phys. D: Appl. Phys. **51**, 273002 (2018).

[61] A. Brataas, Y. V. Nazarov, and G. E. W. Bauer, Eur. Phys. J. B **22**, 99 (2001).

[62] K. Xia, P. J. Kelly, G. E. W Bauer, A. Brataas, and I. Turek, Phys. Rev. B **65**, 220401(R) (2002).

[63] M. Rezende, R. L. Rodrıguez-Suarez, M. M. Soares, L. H. Vilela-Le, D. Ley Domınguez, and A. Azeved, Appl. Phys. Lett. **102**, 012402 (2013).

[64] T. G. A. Verhagen, H. N. Tinkey, H. C. Overweg, M. van Son, M. Huber, J. M. van Ruitenbeek, and J. Aarts, J. Phys.: Condens. Matter **28**, 056004 (2016).

[65] A. Azevedo, L. H. Vilela-Leao, R. L. Rodrıguez-Suarez, A. F. Lacerda Santos, and S. M. Rezende, Phys. Rev. B **83**, 144402 (2011).

[66] S. Emori, U. S. Alaan, M. T. Gray, V. Sluka, Y. Chen, A. D. Kent, and Y. Suzuki, Phys. Rev B **94**, 224423 (2016).

[67] Y. Kajiwara, K. Harii, S. Takahashi, J. Ohe, K. Uchida, M. Mizuguchi, H. Umezawa, H. Kawai, K. Ando, K. Takanashi, S. Maekawa, and E. Saitoh, Nature (London) **464**, 262 (2010).

[68] E. Saitoh, M. Ueda, H. Miyajima, and G. Tatara, Appl. Phys. Lett. **88**, 182509 (2006).

[69] V. A. Atsarkin, I. V. Borisenko, V. V. Demidov, and T. A. Shaikhulov, J. Phys. D: Appl. Phys. **51**, 245002 (2018).

[70] T. A. Shaikhulov, V. V. Demidov, K. L. Stankevich, and G. A. Ovsyannikov, J. Phys. Conf. Ser. **1389**, 012079 (2019).

[71] A. Atsarkin, B. V. Sorokin, I. V. Borisenko, V. V. Demidov, and G. A. Ovsyannikov, J. Phys. D: Appl. Phys. **49**, 125003 (2016).

[72] K. Ando, T. Yoshino, and E. Saitoh, Appl. Phys. Lett. **94**, 152509 (2009).

[73] H. Wang, K.-Y. Meng, P. Zhang, J. T. Hou, J. Finley, J. Han, F. Yang, and L. Liu, Appl. Phys. Lett. **114**, 232406 (2019).

[74] T. Nan, T. J. Anderson, J. Gibbons, K. Hwang, N. Campbell, H. Zhou, Y. Q. Dong, G. Y. Kim, D. F. Shao, T. R. Paudel, N. Reynolds, X. J. Wang, N. X. Sun, E. Y. Tsymbal, S. Y. Choi, M. S. Rzchowski, Y. B. Kim, D. C. Ralph, and C. B. Eom, Proc. Natl. Acad. Sci. U.S.A. **116**, 16186 (2019).

[75] A. S. Everhardt, M. DC, X. Huang, S. Sayed, T. A. Gosavi, Y. Tang, C.-C. Lin, S. Manipatruni, I. A. Young, S. Datta, J.-P. Wang, and R. Ramesh, Phys. Rev. Materials **3**, 051201(R) (2019).

[76] T. M. Vasilevskaya and D. I. Sementsov, Phys. Met. Metallogr. **108**, 321 (2009).